ACS NANO

www.acsnano.org

ARTICLE

Topological Proximity-Induced Dirac Fermion in Two-Dimensional Antimonene

Shu Hsuan Su,[§] Pei-Yu Chuang,[§] Hsin-Yu Chen, Shih-Chang Weng, Wei-Chuan Chen, Ku-Ding Tsuei, Chao-Kuei Lee, Shih-Hsun Yu, Mitch M.-C. Chou, Li-Wei Tu, Horng-Tay Jeng, Chien-Ming Tu, Chih-Wei Luo, Cheng-Maw Cheng,* Tay-Rong Chang,* and Jung-Chun Andrew Huang*

Cite This: *ACS Nano* 2021, 15, 15085−15095

Read Online

ACCESS | Metrics & More | Article Recommendations | Supporting Information

ABSTRACT: **Antimonene is a promising two-dimensional (2D) material that is calculated to have a significant fundamental bandgap usable for advanced applications such as field-effect transistors, photoelectric devices, and the quantum-spin Hall (QSH) state. Herein, we demonstrate a phenomenon termed topological proximity effect, which occurs between a 2D material and a three-dimensional (3D) topological insulator (TI). We provide strong evidence derived from hydrogen etching on Sb_2Te_3 that large-area and well-ordered antimonene presents a 2D topological state. Delicate analysis with a scanning tunneling microscope of the evolutionary intermediates reveals that hydrogen etching on Sb_2Te_3 resulted in the formation of a large area of antimonene with a buckled structure. A topological state formed in the antimonene/Sb_2Te_3 heterostructure was confirmed with angle-resolved photoemission spectra and density-functional theory calculations; in particular, the Dirac point was located almost at the Fermi level. The results reveal that Dirac fermions are indeed realized at the interface of a 2D normal insulator (NI) and a 3D TI as a result of strong hybridization between antimonene and Sb_2Te_3. Our work demonstrates that the position of the Dirac point and the shape of the Dirac surface state can be tuned by varying the energy position of the NI valence band, which modifies the direction of the spin texture of Sb-BL/Sb_2Te_3 *via* varying the Fermi level. This topological phase in 2D-material engineering has generated a paradigm in that the topological proximity effect at the NI/TI interface has been realized, which demonstrates a way to create QSH systems in 2D-material TI heterostructures.**

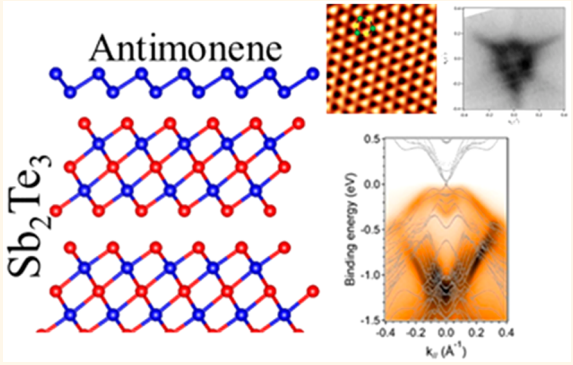

KEYWORDS: *antimonene, topological insulator, normal insulator, scanning tunneling microscope, angle-resolved photoemission spectra*

INTRODUCTION

Three-dimensional (3D) topological insulators (TIs), which refer to the states of matter with an insulating gap in the bulk and gapless helical states on the surface, have attracted much attention due to their fascinating electronic structures. Dictated by time-reversal symmetry, the helical surface states termed mass-less Dirac fermions can move without backscattering on the TI surface.[1−3] Proximity effects that occur in hetero-junctions comprised of TIs and materials can provide an interesting platform to produce emerging quantum phenomena of Dirac fermions at the interfaces. For instance, it has been predicted that a hybrid structure made of a 3D TI and a superconductor can produce a superconducting proximity effect at the interface, which might lead to the emergence of two-dimensional (2D) topological superconductivity hosting Majorana fermions.[4,5] In graphene transferred on 3D TI, a strong proximity effect can induce opening of the band gap and strong spin−orbit coupling (SOC), which leads to a strong tunability and suppression of the spin signal and lifetime.[6,7] There has been some research on the topological proximity effect between a normal insulator and a topological insulator (NI/TI). Previous calculations and experiments have indicated that a Dirac state exists at the NI/TI interface because of the proximity effect caused by TIs.[8−14] In addition, predictions of such an interaction with non-topological states at the NI/TI interface might result in vertical twinning of the Dirac cone; the non-topological states can acquire spin texture without

Received: June 25, 2021
Accepted: August 20, 2021
Published: August 26, 2021

https://doi.org/10.1021/acsnano.1c05454
ACS Nano 2021, 15, 15085−15095

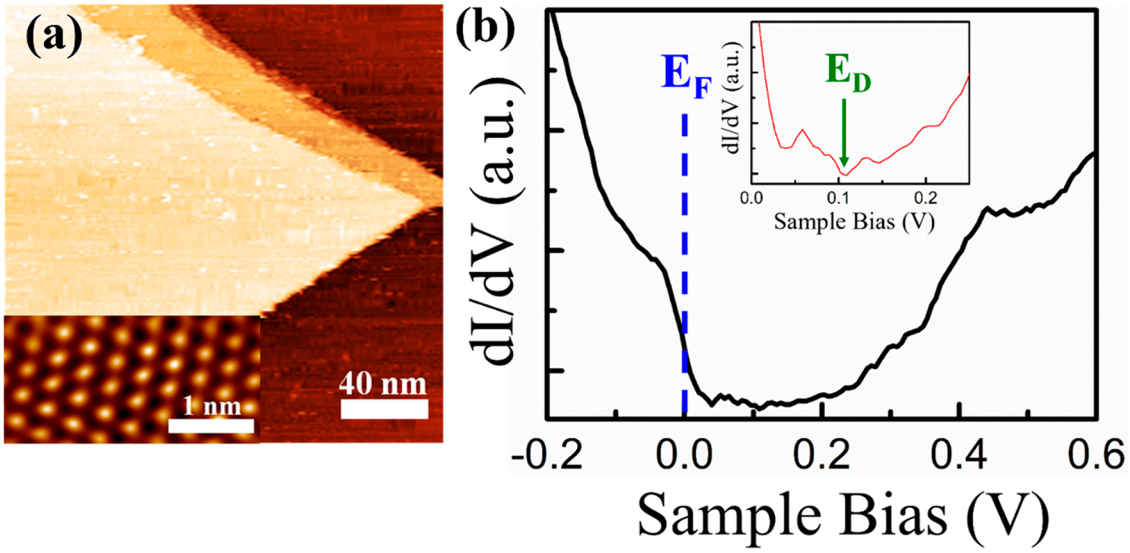

Figure 1. (a) STM image of the cleaved surface of a Sb_2Te_3 single crystal (200 × 200 nm^2, V_S = 0.95 V, I = 0.085 nA). The inset shows an image of the Sb_2Te_3 terrace at atomic resolution (V_S = −0.41 V, I = 0.085 nA). (b) STS spectrum of the Sb_2Te_3 surface (set point: V_S = 0.69 V, I = 0.08 nA). The inset is an enlargement of the STS spectrum at the band gap, and the green arrow indicates the position of the Dirac point.

magnetic doping.[15] The group-V single-element monolayer with a band gap ranging from 0.36 to 2.62 eV on a TI is an ideal platform for the study of the topological proximity effect at a NI/TI interface.[16,17] In particular, the band structure on a 2D NI/3D TI can be directly probed with angle-resolved photoemission spectra (ARPES). The study of the band structure of 2D NI/3D TI is significant for understanding the topological proximity effect; the results bear great potential for spintronics. Furthermore, the interface consisting of 3D TI and 2D materials has recently attracted an investigation of unconventional topological proximity phenomena, such as a topological surface state migrating from the surface of $TlBiSe_2$, and the giant Rashba effect discovered on a Bi (111) bilayer (BL) on Bi_2Se_3.[18−20]

Antimonene is a single elemental 2D material. It was predicted that β-phase antimonene has a significant band gap of about 2.28 eV, which is applicable in field-effect transistors and photoelectric devices.[21−23] It was also predicted that strain engineering would generate significant effects on the electrical transport properties of antimonene, resulting in a quantum-spin Hall (QSH) state.[24−27] β-Antimonene has a buckled honeycomb crystal structure. Various substrates have been used to generate strain to modulate the atomic and band structures of antimonene. For example, it was reported that a honeycomb structure of antimonene grown on Ag (111) is flat with a lattice parameter of about 5.01 Å.[28] Antimonene grown on various substrates such as $PdTe_2$,[29] TIs,[30−34] Ge (111),[35] Pb (111),[36] Cu,[37,38] copper oxide,[39] and Bi[40] has also been reported; these results show that epitaxial growth of antimonene on various substrates allows the electronic properties of these films to be tuned with substrate-induced strain and stress. It should be noted that an ultrathin antimony layer has a drastic evolution of electronic properties from a single layer to several layers thick. Scanning tunneling spectroscopy (STS) mapping of antimony over two BLs shows topological edge states (TESs), which are associated with the observed QSH effect.[37,41]

Antimonene has been synthesized with bottom-up approaches of molecular beam epitaxy (MBE),[28−40] mechanical exfoliation,[42] and chemical vapor deposition (CVD).[43] Except for the MBE method, most antimonene samples encounter small domain sizes, making it difficult to probe the physical properties and to use them for further applications. Even for MBE growth, surface alloys or a phase transition occur spontaneously during the deposition and post-annealing of Sb on the substrate;[36,39,44] obtaining antimonene with a uniform structure remains a challenge. Previous calculations of the band structures of a hybrid structure comprised of Sb and a TI predict a band hybridization of 2D NI and 3D TI,[45] but, so far, the experimental results are lacking.

In this work, smooth and large antimonene was prepared through an atomic hydrogen etching method. We demonstrate a top-down method to prepare antimonene on a Sb_2Te_3 substrate with atomic hydrogen etching. A large, uniform, and flat surface of antimonene can be prepared on a Sb_2Te_3 surface, which was confirmed with scanning tunneling microscopy (STM) and X-ray photoemission spectra (XPS) *in situ*. In our STS study, we observed that the TES is located on the step edge of 2BL antimonene. The band structure of antimonene prepared on Sb_2Te_3 can be detected with ARPES and is consistent with the results of density-functional theory (DFT) calculations. The antimonene-derived spin- polarized bands and the topological surface states have formed a new Dirac cone, of which the Dirac point is almost at the Fermi level. The results reveal that, due to the strong hybridization at the interface between antimonene and Sb_2Te_3, the antimonene/Sb_2Te_3 forms a topologically protected system. A spin spectral-weight calculation on this system shows that the interface state can break the spin helicity and cause the spins to rotate out of the plane of the interface. Our work has demonstrated the manipulation of the topological structure in a 2D NI/3D TI heterostructure comprised of antimonene and Sb_2Te_3. We demonstrate also that the spin texture and the Dirac point can be manipulated in this 2D NI/3D TI system.

RESULTS AND DISCUSSION

Sb_2Te_3 possesses a rhombohedral crystal structure belonging to space group D_{3d}^5 or $R\bar{3}m$.[46,47] The lattice parameters of the

https://doi.org/10.1021/acsnano.1c05454
ACS Nano 2021, 15, 15085−15095

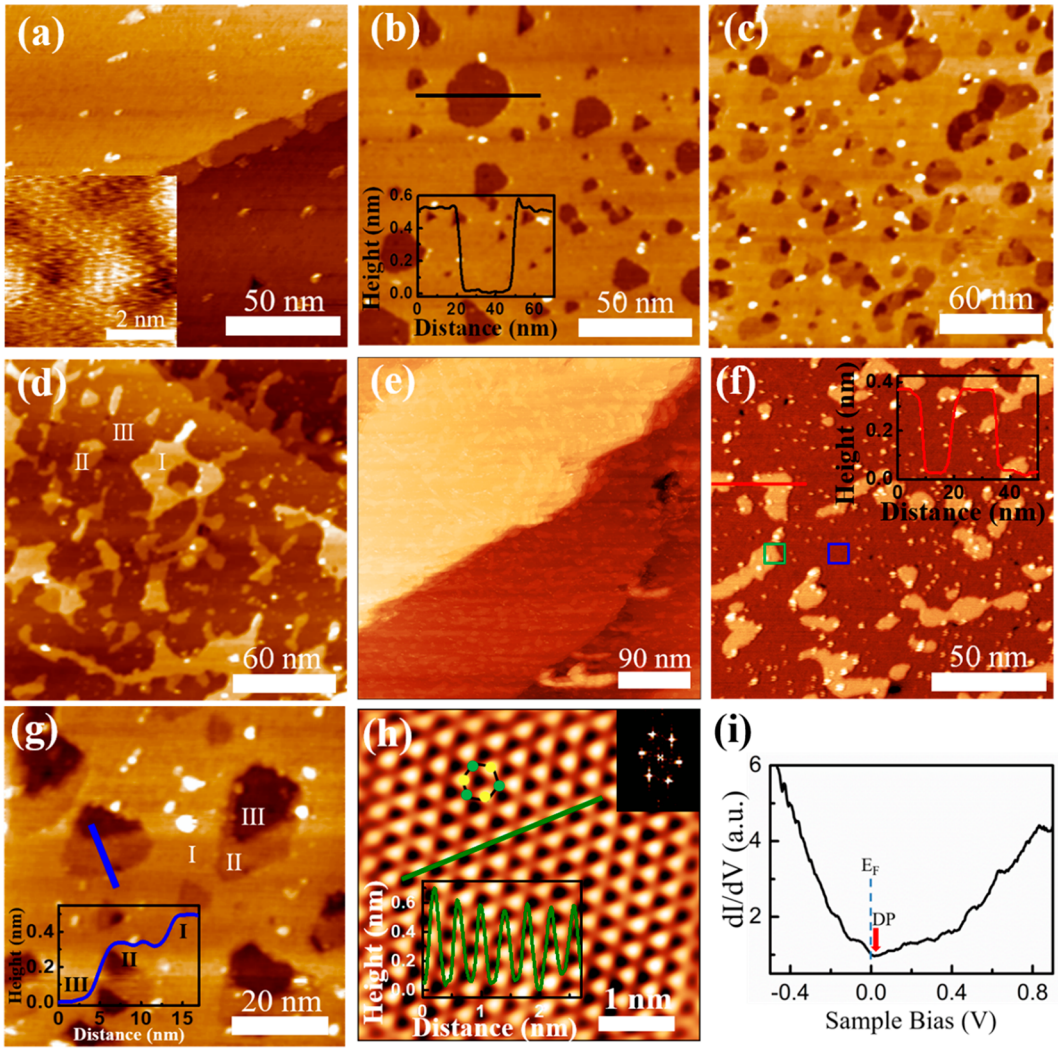

Figure 2. STM images obtained after dosing with hydrogen at (a) 3000 L (150 × 150 nm^2, V_S = 0.89 V, I = 0.085 nA) [the inset shows an atomically resolved close-up view of the terrace (5 × 5 nm^2, V_S = 0.039 V, I = 0.068 nA)]; (b) 6000 L (150 × 150 nm^2, V_S = 1.1 V, I = 0.09 nA) [the inset shows a height profile along the black line at the opening]; (c) 9000 L (200 × 200 nm^2, V_S = 0.89 V, I = 0.08 nA); (d) 12 000 L (200 × 200 nm^2, V_S = 0.89 V, I = 0.1 nA); and (e) 18 000 L (450 × 450 nm^2, V_S = 0.69 V, I = 0.085 nA). Large-scale STM image showing smooth terraces after hydrogen etching. (f) Close-up view of an STM image taken from the terrace in (e) (150 × 150 nm^2, V_S = 0.69 V, I = 0.085 nA) [the inset is a height profile along the red line]. (g) Close-up view of STM topography of the opening section (70 × 70 nm^2, V_S = 1.0 V, I = 0.08 nA) [the inset is a height profile along the blue line]. (h) High-resolution STM image of antimonene (4.5 × 4.5 nm^2, V_S = 0.08 V, I = 0.08 nA) taken from the blue square in (e). A ball-and-stick model is superimposed on the protrusion to indicate the atomic structure. The yellow and green spheres highlight the atomic buckling of antimonene up-and-down such that atoms in the top and bottom layers exhibit bright spots and dark holes in the STM topography, respectively [the inset in the upper right is the corresponding FFT image; the inset in the lower left is the line-scan profile taken along the green line in (g)]. (i) STS spectrum of antimonene/Sb_2Te_3. The red arrow indicates the energetic position of the Dirac point.

Sb_2Te_3 hexagonal unit cell are a = 4.25 Å and c = 30.35 Å. Along the crystallographic direction [111], the unit cell is composed of five atomic layers with stacking sequence Te(1)−Sb−Te(2)−Sb−Te(1), forming a quintuple layer (QL). The coupling is strong within one QL but much weaker between two neighboring QLs, predominantly of van der Waals type.[46,47] As a consequence, the cleaved surface of a bulk Sb_2Te_3 crystal is typically a Te-terminated plane with an unreconstructed (1×1)-Te structure.[48,49] The typical surface morphology of freshly cleaved Sb_2Te_3 is shown in Figure 1a, in which wide terraces separated with regular steps of one QL height (∼1 nm) are visible. The terraces are atomically flat with effective crystallinity, as evident in the magnified image at atomic resolution (inset of Figure 1a), indicating the hexagonal lattice structure of a Te-terminated (111) surface with lattice parameter of about 4.26 Å. The electronic structure of Sb_2Te_3 was probed with STS as shown in Figure 1b, which recorded the differential tunneling conductivity dI/dV and was proportional to the local density of states (LDOS) of the sample.[48,49] The LDOS spectrum shows a bulk band gap of ∼300 meV, for which the energy about 39 meV above E_F can be attributed to the bulk valence band (VB) edge. The enlarged region at the band gap shows a minimum conductance at +108 meV above the Fermi level, indicating the Dirac point (E_D) (identified by an arrow in the inset of Figure 1b), in agreement with previous STS studies,[48−50] confirming the intrinsic *p-type* characterization of the Sb_2Te_3 material.[49,50]

https://doi.org/10.1021/acsnano.1c05454
ACS Nano 2021, 15, 15085−15095

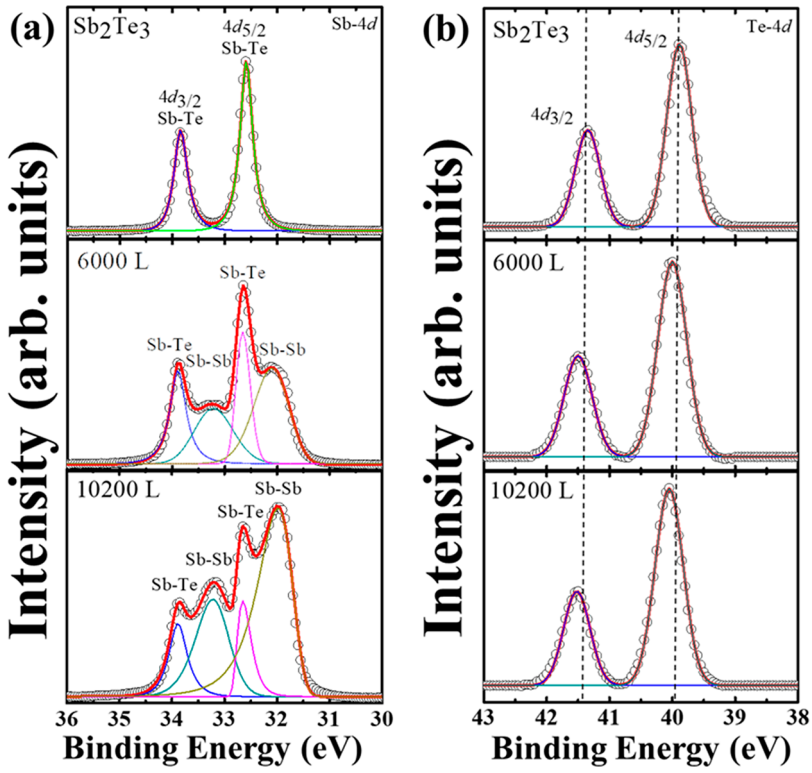

Figure 3. XPS of (a) Sb 4*d* features and (b) Te 4*d* features before and after dosing hydrogen at 0, 6000, and 10 200 L.

STM was employed to study the evolution of the Sb_2Te_3 morphology with increasing hydrogen dose, as shown in Figure 2. The amount of hydrogen atoms initially exposed on the Sb_2Te_3 surface, 3000 L, caused the straight step edges to become wavy step edges, and protrusions (white) formed on the Sb_2Te_3 terraces, as shown in Figure 2a. The atomically resolved STM image (inset of Figure 2a) shows nanoscale pores, indicating that Te vacancies are formed at the top Te (1) level. Some Te atoms might reside above the Te (1) level and form the protrusions. Figure 2b shows the surface morphology after hydrogenation at 6000 L, in which both the protrusions and the triangular and hexagonal openings are evident. The edge orientations of triangular and hexagonal openings are in alignment with the principal crystallographic orientations of the underlying Sb_2Te_3. The line profile in the inset of Figure 2b shows that the step height across the opening is about 5 Å. Note that, after atomic hydrogen etching, most step heights across the openings are below one QL. The formation of a sub-QL step height indicates that the surface has a considerable structural reformation; the top QL Te (1) surface is partially evaporated. As shown in Figure 2c, when the hydrogen dose was further increased to 9000 L, these openings became connected to each other and have irregular shapes. For clarity and the following discussions, a magnified image of Figure 2c is shown in Figure 2g. With hydrogen dose increased to 12 000 L as shown in Figure 2d, the structure inside the openings become more clearly resolved. For convenience, the topmost terraces and the freshly exposed bottom terraces are marked I and III, respectively; the small flat-top terrace in the middle is marked II, as illustrated in Figure 2d,g. We traced a line-profile scan across the opening in the inset of Figure 2g (corresponding to the blue line in Figure 2g), which shows that the height from terrace I to III is about 5 Å, near the spacing between Te (1) and Te (2) layers. Terrace II is about 1.6 Å lower than terrace I and about 3.4 Å higher than terrace III. When the hydrogen dose was increased to 12 000 L, a large fraction of the top Te (1) layer (terrace I) became etched, resulting in residual Te islands on terraces II and III, as shown in Figure 2d. For a hydrogen dose further increased to 18 000 L, the surface revealed the formation of a terrace of large area with some tiny features (~450 nm × 450 nm) in Figure 2e. A magnified STM image at the terrace is shown in Figure 2f. We observed that most of terrace I disappeared and terraces II and III increased until the entire surface was terminated with terrace III, with some residual terrace II. The line scan shown in the inset of Figure 2f (corresponding to the red line in Figure 2f) indicates that the height difference between terraces II and III was maintained at 3.4 Å. This spacing is near the thickness of a single layer of antimonene, which is estimated to be about 3.38 Å.[29] Figure 2h depicts an enlarged STM image of terrace III, designated in blue squares in Figure 2f, revealing a well-ordered, buckled honeycomb structure. Theoretically, antimonene is predicted to have a 2D structure with a buckled honeycomb lattice composed of two sublattices located in separate atomic layers.[16,17,24,25,51] The structure of the buckled honeycomb lattice is revealed by the profile of the lattice, as shown in the inset of Figure 2h (corresponding to the green line in Figure 2h), indicating periodicity of 3.9 Å in the buckled honeycomb lattice. Compared with the lattice of a grown antimonene film with a buckled configuration,[35−37] the lattice parameter of 3.9 Å in this work indicates that the antimonene certainly possesses a higher degree of buckled configuration established on bulk Sb_2Te_3. The corrugation of antimonene formed on hydrogen etching of Sb_2Te_3 agrees satisfactorily with the theoretical calculations.[16,17] The fast-Fourier-transform (FFT) image calculated from Figure 2h clearly shows the periodic spots (inset in upper right of Figure 2h). Figure 2i shows a STS spectrum of antimonene/Sb_2Te_3. We find a

https://doi.org/10.1021/acsnano.1c05454
ACS Nano 2021, 15, 15085−15095

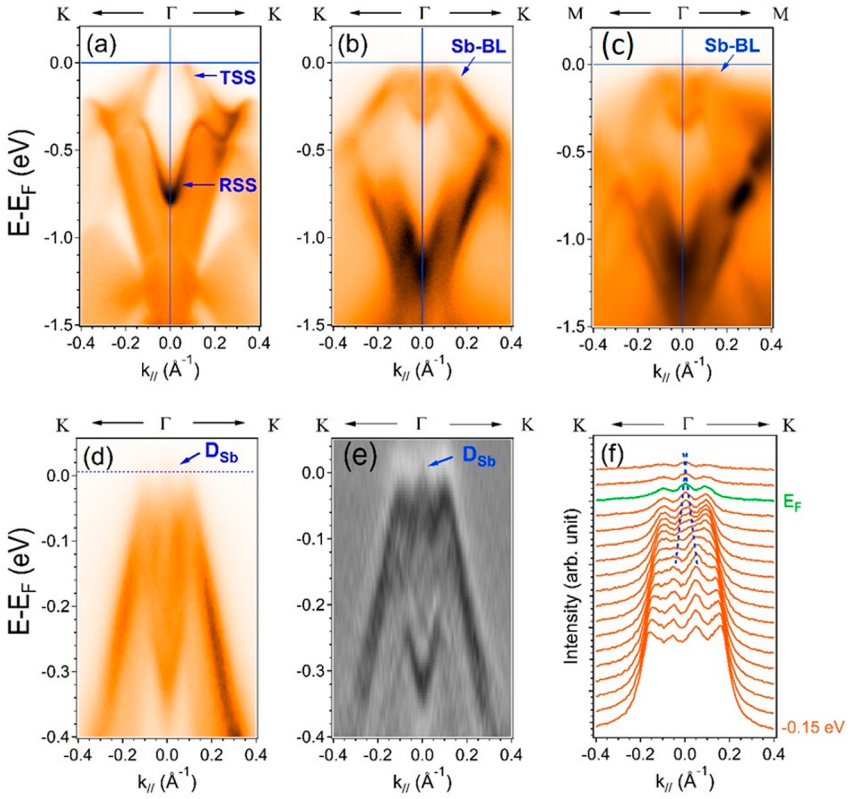

Figure 4. (a) Band-mapping result of Sb_2Te_3 taken at a photon energy of 24 eV. (b) Band-mapping result of antimonene/Sb_2Te_3 along the Γ−K direction taken at a photon energy of 24 eV. (c) Band-mapping result of antimonene/Sb_2Te_3 along the Γ−M direction taken at a photon energy of 24 eV. (d) Enlarged energy scale of the band-mapping result in (b). (e) Corresponding second-derivative plot of (d). (f) Momentum distribution curves (MDCs) of (d), each curve separated by a binding energy of 10 meV.

global minimum, indicating that the Dirac point (marked with red arrow) at +17 mV is located near the Fermi level. Moreover, a nanoisland in terrace II has been singled out and is shown enlarged in Figure S1a. A reasonable deduction of terrace II is hence the initial formation of a 2BL antimonene structure (antimonene nanoislands). The electronic structures of 2BL antimonene can be directly verified with the local differential conductance (dI/dV) spectrum (Figure S1b−e). The STS results confirmed the 1D topological protected edge states of 2BL antimonene. Interestingly, even at a large hydrogen dose, about 24 000 L, the morphology alters little. The formation of antimonene (along with some BL islands) can passivate the surface and prevent further reactions even at large hydrogen doses.

To study the electronic structure of antimonene/Sb_2Te_3 prepared with deliberate atomic hydrogen etching, we conducted XPS and ARPES experiments with varied hydrogen doses to examine the bonding conditions and the evolution of the electronic structure. Figure 3 shows the development of the XPS of Sb 4*d* and Te 5*d* as the hydrogen dose was varied. In pristine Sb_2Te_3, both Sb 4*d* and Te 5*d* show single-component doublets. As shown in Figure 3a, Sb $4d_{3/2}$ and Sb $4d_{5/2}$ orbitals located at 32.7 and 33.9 eV represent Sb−Te bonding, which is consistent with the previous study on Sb_2Te_3.[30,52] As the hydrogen dose was increased to 6000 L, the intensities of the Sb $4d_{3/2}$ and Sb $4d_{5/2}$ signals, characteristic of Sb−Te bonding, were weakened; two other components appeared near 32.1 and 33.3 eV, indicating that Te atoms reacted with H atoms as H_2Te was flushed from the sample surface[53] and Sb atoms remained on the Sb_2Te_3 surface. At a hydrogen dose of 10 200 L, Sb $4d_{3/2}$ and Sb $4d_{5/2}$ doublet Sb−Sb features became more intense than the Sb−Te features. These intense Sb−Sb features indicate that the residual Sb atoms had a large coverage on the Sb_2Te_3 surface. As the hydrogen dose was increased to 15 000 L, the Sb 4*d* intensity ratio of Sb−Sb and Sb−Te seemed not to alter, indicating that the reaction with hydrogen atoms was near saturation. The overall shape of the Sb 5*d* spectrum of hydrogen-etched Sb-BL on Sb_2Te_3 is similar to that of the Sb BL epitaxially grown on Sb_2Te_3.[30] Figure 3b shows the evolution of Te 5*d* as the hydrogen dose was altered. It is noted that, as the hydrogen dose was increased to about 10 200 L, the intensities of the Te 5*d* signals gradually decreased. At hydrogen doses 10 200 and 15 000 L, the Te 5*d* signal intensities were almost unchanged. The corresponding XPS results of Sb 4*d* and Te 5*d* indicate that Sb BL completely covered the surface of Sb_2Te_3, consistent with the STM results. In Figure 3b, note that Sb_2Te_3 after hydrogen etching at dose 15 000 L had a core-level shift of 150 meV to larger binding energy in the Te 5*d* spectrum. This energy shift is attributed to the orbital hybridization existing at the interface between Sb-BL and Sb_2Te_3.

To understand further the change in the electronic structure between Sb_2Te_3 and the antimonene/Sb_2Te_3 hybrid heterostructure, we performed an ARPES experiment to probe the band structures. Figure 4a shows the band-mapping results of pristine Sb_2Te_3 recorded along the Γ−K direction. The topological surface state (TSS) shows a virtually linear band dispersion crossing the Fermi level, forming a Dirac cone. The Dirac point is located above the Fermi level, showing Sb_2Te_3 to be a *p-type* semiconductor, consistent with our STS results

https://doi.org/10.1021/acsnano.1c05454
ACS Nano 2021, 15, 15085−15095

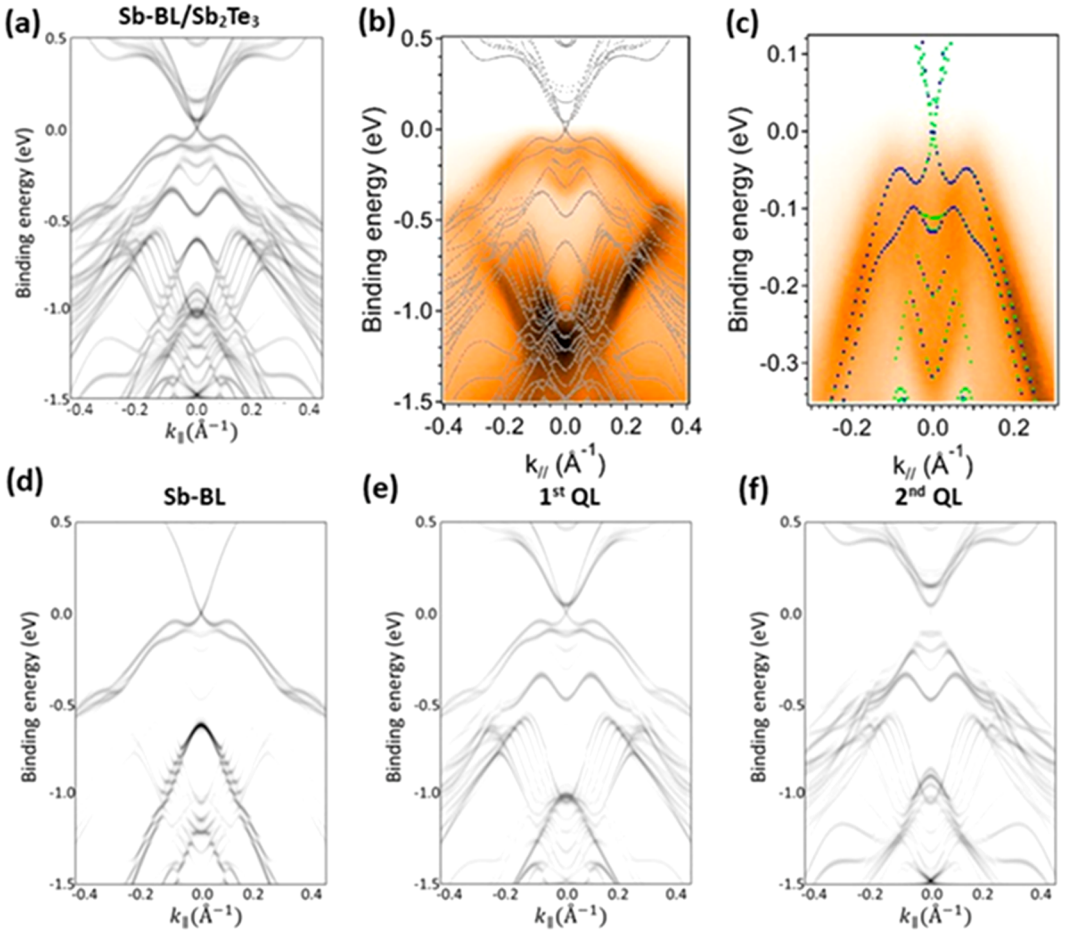

Figure 5. (a) Calculated band structure of Sb-BL/Sb_2Te_3. (b) Overlapping band dispersion extracted from (a) on the band-mapping result of antimonene/Sb_2Te_3. (c) Enlargement of energy and momentum scales in (b). Blue dotted lines represent band dispersions attributed to Sb-BL; green dotted lines represent band dispersions attributed to the first QL of bulk Sb_2Te_3. Spectral weight of the calculated band structure for (d) Sb-BL, (e) first QL, and (f) second QL.

(Figure 1b). The resonance surface state (RSS) can be clearly observed; the orbital hybridization between the TSS and the bulk valence band (BVB) proposed in previous work is also visible in the figure,[54,55] which indicates that the sample was a single crystal of high quality. The extracted $k_F \approx 0.065$ Å^{-1} and $v_F \approx 2.32$ eV Å for TSS are consistent with previous work on Sb_2Te_3.[55] Figure 4b,c displays the band-mapping results of sn antimonene/Sb_2Te_3 hybrid heterostructure along the Γ−K and Γ−M directions, which were recorded at s photon energy of 24 eV. In a comparison of the two band-mapping results along the Γ−K direction between Sb_2Te_3 and antimonene/Sb_2Te_3, an additional Sb-BL-derived band is observed near the Fermi level; the band structure of Sb_2Te_3 has a rigid band shift to a larger binding energy. This band shift is attributed to charge transfer due to orbital hybridization at the interface of Sb_2Te_3 and Sb-BL. This result is also consistent with the observation of the core-level shift of Te 5*d* in the XPS result (Figure 3b). In Figure 4b,c, the band dispersions measured along the Γ−K and Γ−M directions for Sb-BL-derived bands obviously differ, indicating an anisotropic behavior of the Sb-BL-derived bands. In addition, the results of constant energy mapping around the Fermi level show a hexagram-like shape, indicating the existence of a warping effect of the Sb-BL-derived bands (Figure 6h and Figure S3). Figure 4d shows an enlargement of the energy scale in Figure 4b to resolve the band dispersion around the Fermi level. The two Sb-BL-derived bands have an intersection at the Γ point near the Fermi level; a new Dirac point D_{sb} is located almost at the Fermi level. This Dirac cone is confirmed also from the second-derivative plot in Figure 4e and the momentum distribution curves (MDCs) in Figure 4f. The observed band dispersion indicates that a topological state has been formed in the antimonene/Sb_2Te_3 hybrid heterostructure. This Dirac point D_{sb} agrees satisfactorily with the STS result in Figure 2i.

To investigate the topological nature of the Sb-BL/Sb_2Te_3 hybrid system, a representative model is depicted in Figure S4. We calculated the surface spectral weight throughout the (001) surface Brillouin zone (BZ) using the Green's function method, as shown in Figure 5. Figure 5a shows the calculated surface spectral weight with a color corresponding to the integrated charge density of the state within the Sb-BL, topmost QL (first QL, QL1), and the nearest-neighboring QL (second QL, QL2) in Sb_2Te_3. Figure 5b,c displays the wide range and a magnification of the calculated band structures superimposed on the ARPES band mapping, respectively. It is obvious that the calculated result is in excellent agreement with ARPES. As the calculation includes no additional effect, such as impurity or defect or interface reconstruction, the agreement between the calculation and the ARPES supports that the sample quality is quite high. According to the DFT calculations, we identify that the linear Dirac state near E_F is derived from the Sb-BL (Figure 5d). Furthermore, the

https://doi.org/10.1021/acsnano.1c05454
ACS Nano 2021, 15, 15085−15095

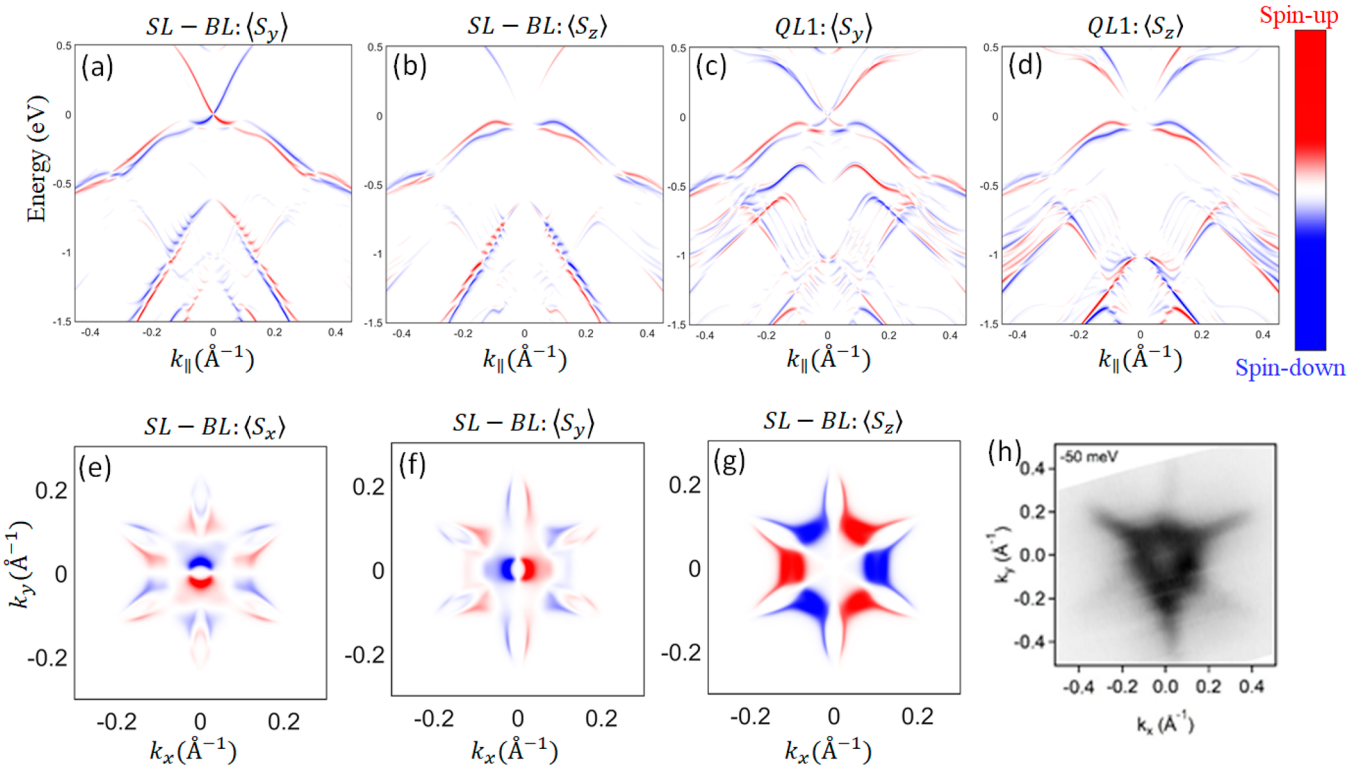

Figure 6. Spin-polarization spectral weight of (a) $\langle S_y \rangle$ spin polarization of Sb-BL, (b) $\langle S_z \rangle$ spin polarization of Sb-BL, (c) $\langle S_y \rangle$ spin polarization of the first QL, and (d) $\langle S_z \rangle$ spin polarization of the first QL. (e−g) Constant-energy contours at energy $E = -50$ meV below E_F with $\langle S_x \rangle$, $\langle S_y \rangle$, and $\langle S_z \rangle$, respectively. (h) Constant-energy contours of ARPES.

intensity of the surface Dirac state decreases rapidly as it enters QL1 (Figure 5e) and QL2 (Figure 5f) in Sb_2Te_3. The residual intensity in QL1 is due to an orbital hybridization that occurs at the interface between Sb-BL and QL1 (Figure 5e). It is worth noting that the free-standing Sb-BL is predicted to be a NI with a band gap of 2.28 eV.[51] The topological Dirac state is thus expected to appear at the interface between NI Sb-BL and TI Sb_2Te_3 in the Sb-BL/Sb_2Te_3 hybrid structure, based on the concept of bulk-boundary correspondence. Surprisingly, our calculations manifest that the topological Dirac state is contributed mainly from the Sb-BL, whereas the band dispersion of QL1 and QL2 in Sb_2Te_3 presents an energy gap. Following the idea of topological band theory, the covered Sb-BL can be effectively regarded as a new surface of the Sb-BL/Sb_2Te_3 hybrid structure. Sb-BL is hence topologicalized because of the proximity effect between Sb-BL and Sb_2Te_3. In previous work,[30] the buckling height in Sb-BL was reported to affect the topological ground state. To clarify this point, we investigated the evolution of the band structure of the free-standing Sb-SL and the Sb-BL/Sb_2Te_3 with varied buckling height. Our calculations show that a modification of the buckling height by 12.5% will not affect the topological ground state of free-standing Sb-SL itself and the Sb-BL/Sb_2Te_3 hybrid structure. The topological Dirac surface state in Sb-BL/Sb_2Te_3 is thus robust. A detailed discussion is shown in Figure S5.

To deepen our understanding of the topological surface state in the Sb-BL/Sb_2Te_3 hybrid structure, we extracted the spin spectral weights in Sb-BL and QL1 as shown in Figure 6. We observed that the spin spectral weights in the Sb-BL near the Fermi level exhibit clear spin-polarized states. The upper cone displays the in-plane spin-texture surrounding $\bar{\Gamma}$ with left-handed chirality, which is similar to the spin texture of the original topological surface state in Sb_2Te_3 (Figure 6a). As expected, the intensity of the spin-polarized Dirac state in QL1 is much less than that in Sb-BL. In addition to the topological surface state, we noticed a quasi-linear spin-polarized band above E_F in QL1. Interestingly, the chirality of its spin texture is opposite that of the Dirac state of Sb-BL. The origin of this unexpected spin-polarized band is difficult to explain with a simple hybridization model, which might be due to the spin splitting of the conduction band on the breaking of spatial inversion symmetry on the interface. Moreover, the Fermi velocity of this quasi-linear band is smaller than that of the Dirac state of Sb-BL. Contrary to the in-plane spin-momentum locked spin-texture, an additional M-shaped out-of-plane S_z spin band appears below E_F in Sb-BL and QL1, which is likely due to a strong warping effect in the hexagonal lattice. This warping feature and the significant out-of-plane spin polarization can also be clearly observed in the spin-polarized constant-energy contour (Figure 6e−g), which is extremely consistent with the ARPES measurement (Figure 6h and Figure S3). As a result, the direction of the spin texture of Sb-BL/Sb_2Te_3 can be greatly modified *via* varying the Fermi level. The changes of spin current caused by Sb-BL were examined with THz circular dichroism spectra (Figure S6).[56,57] The obvious difference in the THz temporal waveforms between Sb_2Te_3 and Sb-BL/Sb_2Te_3 indicates that the spin texture has been significantly tuned. Bilinear magnetotresistance is a suitable experimental method to probe this 3D spin texture, as proposed recently.[58] For the application of spintronic devices, most previous work has focused on the influence of a ferromagnetic layer on the surface of a TI. By effectively using the spin-momentum-locking mechanism in spin-pumping devices, the ballistic conductance of various channels, the

https://doi.org/10.1021/acsnano.1c05454
ACS Nano 2021, 15, 15085−15095

Rashba SOC effect, and the topological surface state are modeled, indicating that the charge current in the TSS channel is independent of energy.[59] Most experiments have shown, however, that bulk insulating TI materials used to decrease the bulk conducting channels can significantly enhance the effect.[60,61]

Besides the pristine topological materials, various NI/TI (or metal/TI) hybrid structures have been proposed and implemented to control both the band dispersion and the energy position of the Dirac point in topological surface states.[18,34,62,63] However, a particular challenge for these materials is that the interface band structure between the adjacent NI and the TI is complicated. In most cases, the Dirac point is far from E_F. In addition, many topologically trivial states cross E_F, diminishing the effectiveness of the spin-polarized current. Searching for a simple topological state in a NI/TI hybrid structure is hence at the frontier of the field. Recent theoretical studies have proposed that the type-II band alignment at the interface between NI and TI, that is, the valence-band maximum of NI, is in the band gap of TI. This may lead to an anti-crossing between the valence state of NI and the Dirac surface state of TI, resulting in a topological surface state that exists in the adjacent NI.[8,10,15] The position of the Dirac point and the shape of the Dirac surface state can consequently be tuned by varying the energy position of the NI valence band, such as altering the doping level. This advantage can be used to manipulate the topological properties of hybrid topological materials. To the best of our knowledge, there is no band structure of a NI/TI hybrid system that satisfies this simple model. We demonstrate that the Sb-BL/Sb_2Te_3 hybrid structure possesses the type-II band alignment, and the induced Dirac surface state agrees qualitatively with the model prediction. Therefore, Sb-BL/Sb_2Te_3 is distinct from other hybrid structures, providing a feasible platform to verify these theoretical models for future development.

CONCLUSION

We have prepared a large and flat antimonene on a Sb_2Te_3 hybrid heterostructure with a top-down method using atomic-hydrogen etching. For this 2D NI/3D TI system, STM/STS, ARPES, and DFT results show that a new topological state is formed; the Dirac point is located almost at the Fermi level as a result of the topological proximity effect induced at the interface between antimonene and Sb_2Te_3. According to the spin-spectral-weight DFT calculations, additional out-of-plane S_z components in the antimonene/Sb_2Te_3 system become predictable, indicating that the spin texture can be modified in the composite NI/TI system. On covering a 2D material on the TI surface, the spin texture and the Dirac point can be tuned. The NI/TI heterostructure provides a promising method for the design of a 2D material/3D TI system to control the direction of spin polarization for spintronic devices. Our results generate a paradigm that demonstrates a way for the creation of a simple and elegant QSH system for spintronics applications.

MATERIALS AND METHODS

Material Growth. Single crystals of Sb_2Te_3 were grown in a homemade resistively heated floating-zone furnace (RHFZ). The initial raw material Sb_2Te_3 was mixed according to the stoichiometric ratios. The stoichiometric mixtures of highly pure elements Sb (99.995%) and Te (99.995%) were first melted at 850−950 °C and then cooled to about 23 °C in an evacuated silica tube. The material served as a feeding rod for the following RHFZ experiment. The growth rate was 1.5 mm/h. After growth, the crystals were cooled to 23 °C over 50 h. Sb_2Te_3 crystals of diameter 3.0 mm and length 30 mm were obtained reproducibly. The crystal cleaved along the basal plane showed a shiny mirror-like surface.

STM and STS Characterization. The STM experiment was performed in an ultrahigh-vacuum (UHV) system (JSPM-4500 A/S; JEOL Ltd.) with base pressure 1.5×10^{-10} Torr. The sample was transferred into a preparation chamber in which samples were cleaved *in situ*. An atomic hydrogen source was used for deliberate hydrogen exposure on the Sb_2Te_3 surface at 100 °C. The details of the hydrogen etching method have been reported in our previous work.[19] To quantify the exposure of the sample, we use the Langmuir (L) unit (1 L = 1.0×10^{-6} Torr·s) in the following. Directly after hydrogen etching, the sample was introduced to the STM measurement chamber under UHV conditions. The STM measurement was the same as in our previous work.[19,64,65] The dI/dV tunneling spectrum was obtained on holding the tip at a fixed distance above the surface and with standard lock-in techniques[64,65] at liquid-nitrogen temperature.

XPS and ARPES Characterization. XPS and ARPES experiments were performed at beamline BL21B1 of Taiwan Light Source (TLS) in National Synchrotron Radiation Research Center (NSRRC). The Sb_2Te_3 single crystal was cleaved *in situ* in an UHV environment before XPS and ARPES measurements. After that, Sb BLs were formed on the Sb_2Te_3 surface with atomic hydrogen etching *in situ* in the upper preparation chamber. The XPS and ARPES measurements have been reported in our previous work.[19] All spectra were recorded at 80 K and a base pressure of 5.6×10^{-11} Torr with incident photon energies of 24 and 58 eV. The overall energy resolution was better than 12 meV.

Computation. The DFT calculations for Sb-BL on the $Sb_2Te_3$6QL slab model were performed on the basis of the generalized gradient approximation (GGA)[66] using the projector augmented-wave method[67] as implemented in the Vienna *ab initio* simulation package (VASP).[68] The experimental lattice parameter (4.25 Å) was applied for the Sb_2Te_3 substrate; the lattice parameter of Sb-BL was constrained to match the substrate. We fixed the Sb_2Te_3 in the bottom four QLs and relaxed the top two QLs and the Sb-BL until the residual forces were less than 0.01 eV/Å. The SOC was included self-consistently in the calculations of electronic structures with a Monkhorst−Pack k-point mesh 15×15×1; the vacuum thickness was greater than 20 Å to ensure the separation of the slabs.

ASSOCIATED CONTENT

Supporting Information

The Supporting Information is available free of charge at https://pubs.acs.org/doi/10.1021/acsnano.1c05454.

Morphology and spectra of edge states of antimonene BL; edge spectral weight in a Sb-BL/Sb_2Te_3-6QL; constant-energy-mapping results of antimonene/Sb_2Te_3; side view of a ball-and-stick model for antimonene/Sb_2Te_3; and THz temporal waveforms of Sb_2Te3, Sb-BL/Sb_2Te_3, and Ge-capped Sb-BL/Sb_2Te_3, including Figures S1−S6 (PDF)

AUTHOR INFORMATION

Corresponding Authors

Cheng-Maw Cheng − *National Synchrotron Radiation Research Center, Hsinchu 300, Taiwan; Department of Physics, National Sun Yat-sen University, Kaohsiung 80424, Taiwan; Taiwan Consortium of Emergent Crystalline Materials, Ministry of Science and Technology, Taipei 10601, Taiwan; Graduate Institute of Applied Science and Technology, National Taiwan University of Science and*

https://doi.org/10.1021/acsnano.1c05454
ACS Nano 2021, 15, 15085−15095

Technology, Taipei 106335, Taiwan; Email: makalu@nsrrc.org.tw

Tay-Rong Chang − *Department of Physics, National Cheng Kung University, Taiwan 701, Taiwan; Center for Quantum Frontiers of Research and Technology (QFort), Tainan 701, Taiwan; Physics Division, National Center for Theoretical Sciences, National Taiwan University, Taipei 10617, Taiwan;* orcid.org/0000-0003-1222-2527; Email: u32trc00@phys.ncku.edu.tw

Jung-Chun Andrew Huang − *Department of Physics, National Cheng Kung University, Taiwan 701, Taiwan; Taiwan Consortium of Emergent Crystalline Materials, Ministry of Science and Technology, Taipei 10601, Taiwan;* orcid.org/0000-0001-6011-0162; Email: jcahuang@mail.ncku.edu.tw

Authors

Shu Hsuan Su − *Department of Physics, National Cheng Kung University, Taiwan 701, Taiwan;* orcid.org/0000-0002-3791-4717

Pei-Yu Chuang − *National Synchrotron Radiation Research Center, Hsinchu 300, Taiwan*

Hsin-Yu Chen − *Department of Physics, National Cheng Kung University, Taiwan 701, Taiwan*

Shih-Chang Weng − *National Synchrotron Radiation Research Center, Hsinchu 300, Taiwan*

Wei-Chuan Chen − *National Synchrotron Radiation Research Center, Hsinchu 300, Taiwan*

Ku-Ding Tsuei − *National Synchrotron Radiation Research Center, Hsinchu 300, Taiwan*

Chao-Kuei Lee − *Department of Photonics and Department of Physics, National Sun Yat-sen University, Kaohsiung 80424, Taiwan; Research Center for Applied Sciences, Academia Sinica, Taipei 11529, Taiwan*

Shih-Hsun Yu − *Department of Materials and Optoelectronics Science, National Sun Yat-sen University, Kaohsiung 80424, Taiwan*

Mitch M.-C. Chou − *Department of Materials and Optoelectronics Science, National Sun Yat-sen University, Kaohsiung 80424, Taiwan*

Li-Wei Tu − *Department of Physics, National Sun Yat-sen University, Kaohsiung 80424, Taiwan*

Horng-Tay Jeng − *Department of Physics, National Tsing Hua University, Hsinchu 30013, Taiwan; Physics Division, National Center for Theoretical Sciences, Hsinchu 30013, Taiwan; Institute of Physics, Academia Sinica, Taipei 11529, Taiwan;* orcid.org/0000-0002-2881-3826

Chien-Ming Tu − *Department of Electrophysics, National Yang Ming Chiao Tung University, Hsinchu 300, Taiwan; Taiwan Consortium of Emergent Crystalline Materials, Ministry of Science and Technology, Taipei 10601, Taiwan*

Chih-Wei Luo − *Department of Electrophysics, National Yang Ming Chiao Tung University, Hsinchu 300, Taiwan; Taiwan Consortium of Emergent Crystalline Materials, Ministry of Science and Technology, Taipei 10601, Taiwan; Institute of Physics, National Yang Ming Chiao Tung University, Hsinchu 300, Taiwan;* orcid.org/0000-0002-6453-7435

Complete contact information is available at: https://pubs.acs.org/10.1021/acsnano.1c05454

Author Contributions

S.H.S. and H.-Y.C. performed STM experiments. P.-Y.C., S.-C.W., W.-C.C., K.-D.T., and C.-M.C. conducted the ARPES experiments. S.-H.Y. and M.M.-C.C. provided single crystals. T.-R.C. performed DFT calculations and theoretical analysis. C.-M.T. and C.-W.L. performed terahertz emission experiments. H.-T.J., C.-K.L., and L.-W.T. assisted the study. C.-M.C., T.-R.C., and J.-C.A.H. wrote and revised the manuscript with input from all authors. All authors discussed the results.

Author Contributions

[§]S.H.S. and P.-Y.C. contributed equally to this work.

Notes

The authors declare no competing financial interest.

ACKNOWLEDGMENTS

The Taiwan Ministry of Science and Technology (MOST) supported this research financially under contracts MOST 107-2119-M-006-016-MY3, 106-2112-M-006-018-MY3, 105-2112-M-213-006-MY2, 107-2112-M-213-001-MY3, 110-2112-M-A49-001-MY3, 106-2112-M-007-012-MY3, 109-2112-M-006−019 -MY3, 109-2112-M-009-020-MY3, and 109-2124-M-009- 003-MY3. H.T.J. also acknowledges support from NCHC, CINC-NTU, AS-iMATE-109-13, and CQT-NTHU-MOE, Taiwan. The National Synchrotron Radiation Research Center (NSRRC) is operated under the Taiwan MOST. T.-R.C. was supported by the Young Scholar Fellowship Program under a MOST grant for the Columbus Program, MOST110-2636-M-006-016, NCKU, Taiwan, and the National Center for Theoretical Sciences, Taiwan. Work at NCKU was supported by the Taiwan MOST under grant MOST107-2627-E-006-001 and the Higher Education Sprout Project, Ministry of Education, to the Headquarters of University Advancement at NCKU.

REFERENCES

(1) Hasan, M. Z.; Kane, C. L. Colloquium: Topological Insulators. *Rev. Mod. Phys.* **2010**, *82*, 3045−3067.

(2) Qi, X.-L.; Zhang, S.-C. Topological Insulators and Superconductors. *Rev. Mod. Phys.* **2011**, *83*, 1057−1110.

(3) Xia, Y.; Qian, D.; Hsieh, D.; Wray, L.; Pal, A.; Lin, H.; Bansil, A.; Grauer, D.; Hor, Y. S.; Cava, R. J.; Hasan, M. Z. Observation of aLarge-Gap Topological-Insulator Class with a SingleDirac Cone on the Surface. *Nat. Phys.* **2009**, *5*, 398−402.

(4) Wang, E.; Ding, H.; Fedorov, A. V.; Yao, W.; Li, Z.; Lv, Y.-F.; Zhao, K.; Zhang, Z.; Xu, L.-G.; Schneeloch, J.; Zhong, R.; Ji, S.-H.; Wang, L.; He, K.; Ma, X.; Gu, G.; Yao, H.; Xue, Q.-K.; Chen, X.; Zhou, S. Fully Gapped Topological Surface States in Bi_2Se_3Films Induced by a d-Wave High-Temperature Superconductor. *Nat. Phys.* **2013**, *9*, 621−625.

(5) Flötotto, D.; Ota, Y.; Bai, Y.; Zhang, C.; Okazaki, K.; Tsuzuki, A.; Hashimoto, T.; Eckstein, J. N.; Shin, S.; Chiang, T.-C. Superconducting Pairing of Topological Surface States in Bismuth SelenideFilms on Niobium. *Sci. Adv.* **2018**, *4*, No. eaar7214.

(6) Khokhriakov, D.; Cummings, A. W.; Song, K.; Vila, M.; Karpiak, B.; Dankert, A.; Roche, S.; Dash, S. P. Tailoring Emergent Spin Phenomena in Dirac Material Heterostructures. *Sci. Adv.* **2018**, *4*, No. eaat9349.

(7) Zhang, J.; Triola, C.; Rossi, E. Proximity Effect in Graphene-Topological-Insulator Heterostructures. *Phys. Rev. Lett.* **2014**, *112*, 096802.

(8) Hutasoit, J. A.; Stanescu, T. D. Induced Spin Texture in Semiconductor/Topological Insulator Heterostructures. *Phys. Rev. B: Condens. Matter Mater. Phys.* **2011**, *84*, 085103.

(9) Wu, G.; Chen, H.; Sun, Y.; Li, X.; Cui, P.; Franchini, C.; Wang, J.; Chen, X.-Q.; Zhang, Z. Tuning the Vertical Location of Helical Surface States in Topological Insulator Heterostructures*via*Dual-ProximityEffects. *Sci. Rep.* **2013**, *3*, 1233.

(10) Men'shov, V. N.; Tugushev, V. V.; Eremeev, S. V.; Echenique, P. M.; Chulkov, E. V. Band Bending Driven Evolution of the BoundElectron States at the Interface between a Three-Dimensional Topological Insulator and a Three-Dimensional Normal Insulator. *Phys. Rev. B: Condens. Matter Mater. Phys.* **2015**, *91*, 075307.
(11) Lee, H.; Yazyev, O. V. Lattice-Matched Heterojunctions between Topological and Normal Insulators: A First-Principles Study. *Phys. Rev. B: Condens. Matter Mater. Phys.* **2017**, *95*, 085304.
(12) Costa, M.; Costa, A. T.; Freitas, W. A.; Schmidt, T. M.; BuongiornoNardelli, M.; Fazzio, A. Controlling Topological States in Topological/Normal Insulator Heterostructures. *ACS Omega* **2018**, *3*, 15900−15906.
(13) Berntsen, M. H.; Goetberg, O.; Wojek, B. M.; Tjernberg, O. Direct Observation of Decoupled Dirac States at the Interface between Topological and Normal Insulators. *Phys. Rev. B: Condens. Matter Mater. Phys.* **2013**, *88*, 195132.
(14) Yoshimi, R.; Tsukazaki, A.; Kikutake, K.; Checkelsky, J. G.; Takahashi, K. S.; Kawasaki, M.; Tokura, Y. Dirac Electron States Formed at the Heterointerface between a Topological Insulator and a Conventional Semiconductor. *Nat. Mater.* **2014**, *13*, 253−257.
(15) Seixas, L.; West, D.; Fazzio, A.; Zhang, S. B. Vertical Twinning of the Dirac Cone at the Interface between Topological Insulators and Semiconductors. *Nat. Commun.* **2015**, *6*, 7630.
(16) Zhang, S.; Xie, M.; Li, F.; Yan, Z.; Li, Y.; Kan, E.; Liu, W.; Chen, Z. F.; Zeng, H. B. Semiconducting Group 15 Monolayers: A Broad Range of Band Gaps and High Carrier Mobilities. *Angew. Chem.* **2016**, *128*, 1698−1701.
(17) Zhang, S.; Guo, S.; Chen, Z.; Wang, Y.; Gao, H.; Gomez-Herrero, J.; Ares, P.; Zamora, F.; Zhu, Z.; Zeng, H. Recent Progress in 2D Group-VA Semiconductors: From Theory to Experiment. *Chem. Soc. Rev.* **2018**, *47*, 982−1021.
(18) Shoman, T.; Takayama, A.; Sato, T.; Souma, S.; Takahashi, T.; Oguchi, T.; Segawa, K.; Ando, Y. Topological Proximity Effect in a Topological Insulator Hybrid. *Nat. Commun.* **2015**, *6*, 6547.
(19) Su, S. H.; Chuang, P.-Y.; Chen, S. W.; Chen, H. Y.; Tung, Y.; Chen, W.-C.; Wang, C.-H.; Yang, Y.-W.; Huang, J. C. A.; Chang, T.-R.; Lin, H.; Jeng, H.-T.; Cheng, C.-M.; Tsuei, K.-D.; Su, H. L.; Wu, Y. C. Selective Hydrogen Etching Leads to 2D Bi(111) Bilayers on Bi_2Se_3: Large Rashba Splitting in Topological Insulator Heterostructure. *Chem. Mater.* **2017**, *29*, 8992−9000.
(20) Sun, R.; Yang, S.; Yang, X.; Vetter, E.; Sun, D.; Li, N.; Su, L.; Li, Y.; Li, Y.; Gong, Z.-Z.; Xie, Z.-K.; Hou, K.-Y.; Gul, Q.; He, W.; Zhang, X.-Q.; Cheng, Z.-H. Large Tunable Spin-to-Charge Conversion Induced by Hybrid Rashba and Dirac Surface States in Topological Insulator Heterostructures. *Nano Lett.* **2019**, *19*, 4420−4426.
(21) Pizzi, G.; Gibertini, M.; Dib, E.; Marzari, N.; Iannaccone, G.; Fiori, G. Performance of Arsenene and AntimoneneDouble-Gate MOSFETs from First Principles. *Nat. Commun.* **2016**, *7*, 12585.
(22) Yin, Y.; Shao, C.; Zhang, C.; Zhang, Z.; Zhang, X.; Robertson, J.; Guo, Y. Anisotropic Transport Property of Antimonene MOSFETs. *ACS Appl. Mater. Interfaces* **2020**, *12*, 22378−22386.
(23) Xiao, Q.; Hu, C.-X.; Wu, H.-R.; Ren, Y.-Y.; Li, X.-Y.; Yang, Q.-Q.; Dun, G.-H.; Huang, Z.- P.; Peng, Y.; Yan, F.; Wang, Q.; Zhang, H.-L. Antimonene-Based Flexible Photodetector. *Nanoscale Horiz.* **2020**, *5*, 124−130.
(24) Chuang, F.-C.; Hsu, C.-H.; Chen, C.-Y.; Huang, Z.-Q.; Ozolins, V.; Lin, H.; Bansil, A. Tunable Topological Electronic Structures in Sb(111) Bilayers: A First-Principles Study. *Appl. Phys. Lett.* **2013**, *102*, 022424.
(25) Wang, G.; Pandey, R.; Karna, S. P. Atomically Thin Group V Elemental Films: Theoretical Investigations of Antimonene Allotropes. *ACS Appl. Mater. Interfaces* **2015**, *7*, 11490−11496.
(26) Zhao, M.; Zhang, X.; Li, L. Strain-Driven Band Inversion and Topological Aspects in Antimonene. *Sci. Rep.* **2015**, *5*, 16108.
(27) Aktürk, O. Ü.; Özçelik, V. O.; Ciraci, S. Single-Layer Crystalline Phases of Antimony: Antimonenes. *Phys. Rev. B: Condens. Matter Mater. Phys.* **2015**, *91*, 235446.
(28) Shao, Y.; Liu, Z.-L.; Cheng, C.; Wu, X.; Liu, H.; Liu, C.; Wang, J.-O.; Zhu, S.-Y.; Wang, Y.-Q.; Shi, D.-X.; Ibrahim, K.; Sun, J.-T.; Wang, Y.-L.; Gao, H.-J. Epitaxial Growth of Flat Antimonene Monolayer: A New Honeycomb Analogue of Graphene. *Nano Lett.* **2018**, *18*, 2133−2139.
(29) Wu, X.; Shao, Y.; Liu, H.; Feng, Z.; Wang, Y. L.; Sun, J. T.; Liu, C.; Wang, J. O.; Liu, Z. L.; Zhu, S. Y.; Wang, Y. Q.; Du, S. X.; Shi, Y. G.; Ibrahim, K.; Gao, H. J. Epitaxial Growth and Air-Stability of Monolayer Antimonene on $PdTe_2$. *Adv. Mater.* **2017**, *29*, 1605407.
(30) Lei, T.; Liu, C.; Zhao, J.-L.; Li, J.-M.; Li, Y.-P.; Wang, J.-O.; Wu, R.; Qian, H.-J.; Wang, H.-Q.; Ibrahim, K. Electronic Structure of Antimonene Grown on Sb_2Te_3 (111) and Bi_2Te_3 Substrates. *J. Appl. Phys.* **2016**, *119*, 015302.
(31) Flammini, R.; Colonna, S.; Hogan, C.; Mahatha, S. K.; Papagno, M.; Barla, A.; Sheverdyaeva, P. M.; Moras, P.; Aliev, Z. S.; Babanly, M. B.; Chulkov, E. V.; Carbone, C.; Ronci, F. Evidence of β-Antimonene at the Sb/Bi_2Se_3 Interface. *Nanotechnology* **2018**, *29*, 065704.
(32) Lei, T.; Li, J.-M.; Li, F.-S.; Wang, J.-O.; Ibrahim, K.; Zhang, K. Anisotropic Electronic Structure of Antimonene. *Appl. Phys. Lett.* **2019**, *115*, 221602.
(33) Hogan, C.; Holtgrewe, K.; Ronci, F.; Colonna, S.; Sanna, S.; Moras, P.; Sheverdyaeva, P. M.; Mahatha, S.; Papagno, M.; Aliev, Z. S.; Babanly, M.; Chulkov, E. V.; Carbone, C.; Flammini, R. Temperature Driven Phase Transition at the Antimonene/Bi_2Se_3 van der Waals Heterostructure. *ACS Nano* **2019**, *13*, 10481−10489.
(34) Holtgrewe, K.; Mahatha, S. K.; Sheverdyaeva, P. M.; Moras, P.; Flammini, R.; Colonna, S.; Ronci, F.; Papagno, M.; Barla, A.; Petaccia, L.; Aliev, Z. S.; Babanly, M. B.; Chulkov, E. V.; Sanna, S.; Hogan, C.; Carbone, C. Topologization of β-Antimonene on Bi_2Se_3 *via* Proximity effects. *Sci. Rep.* **2020**, *10*, 14619.
(35) Fortin-Deschenes, M.; Waller, O.; Mentes, T. O.; Locatelli, A.; Mukherjee, S.; Genuzio, F.; Levesque, P. L.; Hebert, A.; Martel, R.; Moutanabbir, O. Synthesis of Antimonene on Germanium. *Nano Lett.* **2017**, *17*, 4970−4975.
(36) Jałochowski, M.; Krawiec, M. Antimonene on PbQuantum Wells. *2D Mater.* **2019**, *6*, 045028.
(37) Niu, T.; Zhou, W.; Zhou, D.; Hu, X.; Zhang, S.; Zhang, K.; Zhou, M.; Fuchs, H.; Zeng, H. Modulating Epitaxial Atomic Structure of Antimonenethrough Interface Design. *Adv. Mater.* **2019**, *31*, 1902606.
(38) Zhu, S. Y.; Shao, Y.; Wang, E.; Cao, L.; Li, X.-Y.; Liu, Z.-L.; Liu, C.; Liu, L.-W.; Wang, J.-O.; Ibrahim, K.; Sun, J.-T.; Wang, Y.-L.; Du, S.; Gao, H. J. Evidence of Topological Edge States in Buckled Antimonene Monolayers. *Nano Lett.* **2019**, *19*, 6323−6329.
(39) Niu, T. C.; Meng, Q. L.; Zhou, D. C.; Si, N.; Zhai, S. W.; Hao, X. M.; Zhou, M.; Fuchs, H. Large-Scale Synthesis of Strain-Tunable Semiconducting Antimonene on Copper Oxide. *Adv. Mater.* **2020**, *32*, 1906873.
(40) Markl, T.; Kowalczyk, P. J.; Le Ster, M.; Mahajan, I. V.; Pirie, H.; Ahmed, Z.; Bian, G.; Wang, X.; Chiang, T.-C.; Brown, S. A. Engineering Multiple Topological Phases in Nanoscalevan der Waals Heterostructures: Realisation of α-Antimonene. *2D Mater.* **2018**, *5*, 011002.
(41) Kim, S. H.; Jin, K. H.; Park, J.; Kim, J. S.; Jhi, S. H.; Yeom, H. W. Topological Phase Transition and Quantum Spin Hall Edge States of Antimony Few Layers. *Sci. Rep.* **2016**, *6*, 33193.
(42) Ares, P.; Aguilar-Galindo, F.; Rodríguez-San-Miguel, D.; Aldave, D. A.; Díaz-Tendero, S.; Alcamí, M.; Martín, F.; Gomez-Herrero, J.; Zamora, F. Mechanical Isolation of Highly Stable Antimonene under Ambient Conditions. *Adv. Mater.* **2016**, *28*, 6332−6336.
(43) Ji, J.; Song, X.; Liu, J.; Yan, Z.; Huo, C.; Zhang, S.; Su, M.; Liao, L.; Wang, W.; Ni, Z.; Hao, Y.; Zeng, H. Two-Dimensional AntimoneneSingle Crystals Grown by van der Waals Epitaxy. *Nat. Commun.* **2016**, *7*, 13352.
(44) Mao, Y. H.; Zhang, L. F.; Wang, H. L.; Shan, H.; Zhai, X. F.; Hu, Z. P.; Zhao, A. D.; Wang, B. Epitaxial Growth of Highly Strained Antimonene On Ag(111). *Front. Phys.* **2018**, *13*, 138106.

https://doi.org/10.1021/acsnano.1c05454
ACS Nano 2021, 15, 15085−15095

(45) Jin, K.-H.; Yeom, H. W.; Jhi, S.-H. Band Structure Engineering of Topological Insulator Heterojunctions. *Phys. Rev. B: Condens. Matter Mater. Phys.* **2016**, *93*, 075308.
(46) Anderson, T. L.; Krause, H. B. Refinement of the Sb_2Te_3 and Sb_2Te_2Se Structures and Their Relationship to Nonstoichiometric $Sb_2Te_{3-y}Se_y$Compounds. *Acta Crystallogr., Sect. B: Struct. Crystallogr. Cryst. Chem.* **1974**, *30*, 1307−1310.
(47) Teramoto, I.; Takayanagi, S. Relations between the Electronic Properties and the Chemical Bonding of $Sb_xBi_{2-x}Te_{3-y}Se_y$ System. *J. Phys. Chem. Solids* **1961**, *19*, 124−129.
(48) Sessi, P.; Storz, O.; Bathon; Wilfert, T. S.; Kokh, K. A.; Tereshchenko, O. E.; Bihlmayer, G.; Bode, M. Scattering Properties of the Three-Dimensional Topological Insulator Sb_2Te_3: Coexistence of Topologically Trivial and Nontrivial Surface States with Opposite Spin-Momentum Helicity. *Phys. Rev. B: Condens. Matter Mater. Phys.* **2016**, *93*, 035110.
(49) Zhang, W.; West, D.; Lee, S. H.; Qiu, Y.; Chang, C.-Z.; Moodera, J. S.; Hor, Y. S.; Zhang, S.; Wu, W. Electronic Fingerprints of Cr and V Dopants in the Topological Insulator Sb_2Te_3. *Phys. Rev. B: Condens. Matter Mater. Phys.* **2018**, *98*, 115165.
(50) Li, C. H.; van'tErve, O. M. J.; Li, Y. Y.; Li, L.; Jonker, B. T. Electrical Detection of the HelicalSpin Texture in a *p-Type* TopologicalInsulator Sb_2Te_3. *Sci. Rep.* **2016**, *6*, 29533.
(51) Zhang, S.; Yan, Z.; Li, Y.; Chen, Z.; Zeng, H. Atomically Thin Arsenene and Antimonene: Semimetal-Semiconductor and Indirect-Direct BandGap Transitions. *Angew. Chem.* **2015**, *127*, 3155−3158.
(52) Volykhov, A. A.; Sanchez-Barriga, J.; Sirotina, A. P.; Neudachina, V. S.; Frolov, A. S.; Gerber, E. A.; Kataev, E. Y.; Senkovsky, B.; Khmelevsky, N. O.; Aksenenko, A. Y.; Korobova, N. V.; Knop-Gericke, A.; Rader, O.; Yashina, L. V. Rapid Surface Oxidation of Sb_2Te_3 as Indication for a Universal Trend in the Chemical Reactivity of Tetradymite Topological Insulators. *Chem. Mater.* **2016**, *28*, 8916−8923.
(53) Zhang, K.-W.; Ding, D.; Yang, C.-L.; Gan, Y.; Li, S.; Huang, W.-K.; Song, Y.-H.; Jia, Z.-Y.; Li, X.-B.; Zhu, Z.; Wen, J.; Chen, M.; Li, S.-C. Real-Space Characterization of Reactivity towards Water at the Bi_2Te_3(111) Surface. *Phys. Rev. B: Condens. Matter Mater. Phys.* **2016**, *93*, 235445.
(54) Pauly, C.; Bihlmayer, G.; Liebmann, M.; Grob, M.; Georgi, A.; Subramaniam, D.; Scholz, M. R.; Sanchez-Barriga, J.; Varykhalov, A.; Blügel, S.; Rader, O.; Morgenstern, M. Probing Two Topological Surface Bands of Sb_2Te_3 by Spin-Polarized Photoemission Spectroscopy. *Phys. Rev. B: Condens. Matter Mater. Phys.* **2012**, *86*, 235106.
(55) Seibel, C.; Bentmann, H.; Braun, J.; Minar, J.; Maaß, H.; Sakamoto, K.; Arita, M.; Shimada, K.; Ebert, H.; Reinert, F. Connection of a Topological Surface State with the Bulk Continuum in Sb_2Te_3 (0001). *Phys. Rev. Lett.* **2015**, *114*, 066802.
(56) Tu, C.-M.; Chen, Y.-C.; Huang, P.; Chuang, P.-Y.; Lin, M.-Y.; Cheng, C.-M.; Lin, J.-Y.; Juang, J.-Y.; Wu, K.-H.; Huang, J.-C. A.; Pong, W.-F.; Kobayashi, T.; Luo, C.-W. Helicity-Dependent Terahertz Emission Spectroscopy of Topological Insulator Sb_2Te_3 Thin Films. *Phys. Rev. B: Condens. Matter Mater. Phys.* **2017**, *96*, 195407.
(57) Chen, X.; Wang, H.; Wang, C.; Ouyang, C.; Wei, G.; Nie, T.; Zhao, W.; Miao, J.; Li, Y.; Wang, L.; Wu, X. Efficient Generation and Arbitrary Manipulation of Chiral Terahertz Waves Emitted from Bi_2Te_3-Fe Heterostructures. *Adv. Photonics Res.* **2021**, *2*, 2000099.
(58) He, P.; Zhang, S. S. L.; Zhu, D.; Liu, Y.; Wang, Y.; Yu, J.; Vignale, G.; Yang, H. Bilinear Magnetoelectric Resistance as a Probe of Three-Dimensional Spin Texture in Topological Surface States. *Nat. Phys.* **2018**, *14*, 495−499.
(59) Hong, S.; Diep, V.; Datta, S.; Chen, Y. P. Modeling Potentiometric Measurements in Topological Insulators Including Parallel Channels. *Phys. Rev. B: Condens. Matter Mater. Phys.* **2012**, *86*, 085131.
(60) Ando, Y.; Hamasaki, T.; Kurokawa, T.; Ichiba, K.; Yang, F.; Novak, M.; Sasaki, S.; Segawa, K.; Ando, Y.; Shiraishi, M. Electrical Detection of the Spin Polarization Due to Charge Flow in the Surface State of the Topological Insulator $Bi_{1.5}Sb_{0.5}Te_{1.7}Se_{1.3}$. *Nano Lett.* **2014**, *14*, 6226−6230.
(61) Kondou, K.; Yoshimi, R.; Tsukazaki, A.; Fukuma, Y.; Matsuno, J.; Takahashi, K. S.; Kawasaki, M.; Tokura, Y.; Otani, Y. Fermi-Level-Dependent Charge-to-Spin Current Conversion by Dirac Surface States of Topological Insulators. *Nat. Phys.* **2016**, *12*, 1027−1031.
(62) Kim, S. H.; Jin, K.-H.; Park, J.; Kim, J. S.; Jhi, S.-H.; Kim, T.-H.; Yeom, H. W. Edge and Interfacial States in a Two-Dimensional Topological Insulator: Bi(111) Bilayer on Bi_2Te_2Se. *Phys. Rev. B: Condens. Matter Mater. Phys.* **2014**, *89*, 155436.
(63) Trang, C. X.; Shimamura, N.; Nakayama, K.; Souma, S.; Sugawara, K.; Watanabe, I.; Yamauchi, K.; Oguchi, T.; Segawa, K.; Takahashi, T.; Ando, Y.; Sato, T. Conversion of a Conventional Superconductor into a Topological Superconductor by Topological Proximity Effect. *Nat. Commun.* **2020**, *11*, 159.
(64) Chen, H.-H.; Su, S. H.; Chang, S.-L.; Cheng, B.-Y.; Chong, C.-W.; Huang, J. C. A.; Lin, M.-F. Long-Range Interactions of Bismuth Growth on Monolayer Epitaxial Graphene at Room Temperature. *Carbon* **2015**, *93*, 180−186.
(65) Chen, H.-H.; Su, S. H.; Chang, S.-L.; Cheng, B.-Y.; Chen, S. W.; Chen, H.-Y.; Lin, M.-F.; Huang, J. C. A. Tailoring Low-Dimensional Structures of Bismuth on Monolayer Epitaxial Graphene. *Sci. Rep.* **2015**, *5*, 11623.
(66) Perdew, J. P.; Burke, K.; Ernzerhof, M. Generalized Gradient Approximation Made Simple. *Phys. Rev. Lett.* **1996**, *77*, 3865−3868.
(67) Blöchl, P. E. Projector Augmented-Wave Method. *Phys. Rev. B: Condens. Matter Mater. Phys.* **1994**, *50*, 17953.
(68) Kresse, G.; Hafner, J. *abInitio* Molecular Dynamics for Open-Shell Transition Metals. *Phys. Rev. B: Condens. Matter Mater. Phys.* **1993**, *48*, 13115−13118.

https://doi.org/10.1021/acsnano.1c05454
ACS Nano 2021, 15, 15085−15095